

Static stress drop associated with brittle slip events on exhumed faults

W. A. Griffith,^{1,2} G. Di Toro,^{3,4} G. Pennacchioni,^{3,4} D. D. Pollard,¹ and S. Nielsen⁴

Received 17 June 2008; revised 5 November 2008; accepted 15 December 2008; published 21 February 2009.

[1] We estimate the static stress drop on small exhumed strike-slip faults in the Lake Edison granodiorite of the central Sierra Nevada (California). The subvertical strike-slip faults were exhumed from 4 to 15 km depth and were chosen because they are exposed in outcrop along their entire tip-to-tip lengths of 8–12 m. Slip nucleated on joints and accumulated by crystal-plastic shearing (forming quartz mylonites from early quartz vein filling in joints) and successive brittle faulting (forming epidote-bearing cataclasites). The occurrence of thin, $\leq 300 \mu\text{m}$ wide, pseudotachylytes along some small faults throughout the study area suggests that some, if not all, of the brittle slip on the study area faults may have been seismic. We suggest that the contribution of brittle, cataclastic slip to the total slip along the studied cataclasite-bearing small faults may be estimated by the length of epidote-filled, rhombohedral dilatational jogs (rhombochasms) distributed quasi-periodically along the length of the faults. The interpretation that slip recorded by rhombochasms occurred in single events is based on evidence that (1) epidote crystals are randomly oriented and undeformed within the rhombochasm; (2) cataclasite in principal slip zones does not include clasts of previous cataclasite, and (3) rhombochasm lengths vary systematically along the length of the faults with slip maximum occurring near the fault center, tapering to the fault tips. We thereby constrain both the rupture length and slip. On the basis of these measurements, we calculate stress drops ranging over 90–250 MPa, i.e., one to two orders of magnitude larger than typical seismological estimates for earthquakes, but similar in magnitude to seismological estimates of small (M_2) earthquakes from the San Andreas Fault Observatory at Depth (SAFOD). The slip events described in the present study occurred along small, deep-seated faults, and, given the calculated stress drops and observations that brittle faults exploited joints sealed by quartz-bearing mylonite, we conclude that these were “strong” faults.

Citation: Griffith, W. A., G. Di Toro, G. Pennacchioni, D. D. Pollard, and S. Nielsen (2009), Static stress drop associated with brittle slip events on exhumed faults, *J. Geophys. Res.*, 114, B02402, doi:10.1029/2008JB005879.

1. Introduction

[2] The static shear stress drop associated with earthquakes is a fundamental quantity that scales linearly with slip, particle velocity, and acceleration [Scholz, 2002] and is typically calculated using a characteristic source dimension (e.g., fault radius for a circular fault), average slip, and the estimated shear modulus of the host rock. The stress drop ($\Delta\sigma$) is defined as the difference between σ'_{zx} , the peak shear stress in the remote field, and σ'_{zx} , the shear stress resolved on the fault after slip, where slip is in the x direction and z is normal to the fault. Kanamori [1994] distinguishes two end-member characteristic faults based on the stress σ'_{zx} at which

they fail: (1) weak faults for which $\sigma'_{zx} \approx 20$ MPa and (2) strong faults for which $\sigma'_{zx} \approx 200$ MPa.

[3] Stress drops measured in triaxial experiments of shear failure of intact rocks are typically on the order of hundreds of MPa to GPa [e.g., Brace and Byerlee, 1966]. Triaxial experiments with sawcut samples have yielded slightly smaller stress drops in the range from tens to hundreds of MPa [Brace and Byerlee, 1966]. These results indicate that, at least in the laboratory, faults in geomaterials are strong. In both types of experiments, the shear stress drop was a fraction of the peak yield stress; however, stress drops on the order of hundreds of MPa in the upper crust would constitute a near total stress drop ($\sigma'_{zx} \approx 0$). Laboratory stress drops stand in stark contrast to seismologically observed stress drops, typically on the order of 0.1–100 MPa, a fraction of the shear strength of intact rock at seismogenic depths [e.g., Kanamori, 1994; Abercrombie, 1995].

[4] The earthquake rupture process has long been considered to follow a self-similar scaling relationship, as stress drop has been observed to be independent of magnitude [Aki, 1967]; however, this scale independence has been observed to break down for earthquakes below $M_L \sim 3$, as small

¹Department of Geological and Environmental Sciences, Stanford University, Stanford, California, USA.

²Now at Istituto Nazionale di Geofisica e Vulcanologia, Rome, Italy.

³Dipartimento di Geoscienze, Università di Padova, Padua, Italy.

⁴Istituto Nazionale di Geofisica e Vulcanologia, Rome, Italy.

earthquakes appear to be associated with smaller stress drops [e.g., *Archuleta et al.*, 1982; *Hanks*, 1982; *Guo et al.*, 1992]. Minimum source dimensions on the order of 100 m have been inferred for earthquakes, offering one solution for the apparent deviation in scaling [*Archuleta et al.*, 1982, *Guo et al.*, 1992]. If 100 m is truly a minimum source dimension (presumably controlled by geometry or nucleation length), then smaller observed moments must be attributed to lower values of average fault slip leading to smaller calculated stress drops. More recently, however, this breakdown in scaling for small earthquakes has been established to be an artifact of severe near surface attenuation of high frequency waves [e.g., *Hanks*, 1982]. Attenuation of high-frequency waves artificially distorts the amplitude spectrum, making interpretation of the corner frequency difficult [e.g., *Hanks*, 1982; *Hough and Anderson*, 1988; *Abercrombie*, 1995; *Prejean and Ellsworth*, 2001].

[5] Researchers have attempted to circumvent the problem of small source resolution by examining data recorded by seismometers closer to the source, in deep boreholes [*Abercrombie*, 1995], or in deep South African gold mines [e.g., *Richardson and Jordan*, 2002]. Recent studies suggest that using borehole seismometers may not effectively alleviate problems with high-frequency attenuation [*Ide and Beroza*, 2001; *Imanishi and Ellsworth*, 2006]. Using a stable spectral ratio method to analyze microearthquakes from the San Andreas Fault Observatory at Depth (SAFOD) seismic array in Parkfield, California, *Imanishi and Ellsworth* [2006] showed that there is no scaling breakdown for stress drop or apparent stress and found that half of the microearthquakes examined had static stress drops greater than 10 MPa.

[6] An alternative approach to studying the source of small earthquakes, which effectively removes any spatial ambiguity introduced by inferring earthquake source dimensions, is to study the earthquake source by direct examination of ancient earthquake ruptures along faults exhumed from hypocentral depths. Detailed investigation of faults at the outcrop and microscopic scale can resolve to high precision the spatial extent and geometry of rupture in two dimensions and the fault slip. Given these parameters and the shear modulus of the fault host rocks the stress drop can be calculated with the same elastic dislocation models commonly employed by earthquake seismologists. Unfortunately, such estimates have been difficult to come by because a number of factors need to be present in outcrop to successfully estimate the stress drop:

[7] 1. The fault must be exposed along its entire length in order to measure the source dimension, and the fault must be isolated from nearby faults to lessen the potential for fault interaction.

[8] 2. Slip must be measured for a single slip event.

[9] 3. Evidence of seismic slip must be present if the slip is interpreted to be related to ancient earthquakes. For exhumed faults, this means that pseudotachylite (solidified friction-induced melts produced during seismic slip [*Sibson*, 1975]) must be present within the slipping zone [*Cowan*, 1999].

[10] Complete slip distributions have been measured along the entire length of faults exposed at the Earth's surface via remote sensing and field mapping [e.g., *Maerten et al.*, 2001; *Manighetti et al.*, 2001], and 3-D seismic data

sets [e.g., *Willemse*, 1997; *Kattenhorn and Pollard*, 2001]. Slip estimates along small exhumed faults most typically consist of sparse (one or two) measurements of piercing points along the fault representing only the relative particle displacement at the point of measurement [e.g., *Shipton et al.*, 2006]. With few exceptions [e.g., *Di Toro et al.*, 2005, 2006], slip measurements along natural faults almost always represent the total accumulated slip (representing multiple slip episodes) during the history of fault activity.

[11] Here we attempt to use geological observations to calculate the stress drops for slip events along small exhumed faults by describing deformation associated with single slip events which can be mapped in two dimensions from one tip of the fault to the other. The results of these calculations are compared to data from the seismological record. This approach effectively removes ambiguity about the source dimensions and geometry inherent in the seismological inverse problem by affording direct observation of the source.

2. Bear Creek Faults

[12] Fracturing and faulting has been documented in the Bear Creek drainage, in the southern half of the Mount Abbot quadrangle in the Sierra Nevada batholith [e.g., *Lockwood and Lydon*, 1975; *Segall and Pollard*, 1983a, 1983b; *Martel et al.*, 1988; *Pachell and Evans*, 2002]. These studies have concentrated on the Lake Edison Granodiorite (~88 Ma) whose depth of emplacement is estimated at 4–15 km based on amphibole geobarometry [*Ague and Brimhall*, 1988]. K-Ar ages from muscovite in the fractures date the Bear Creek faults at 79 Ma, and these faults have been interpreted as having grown soon after pluton emplacement [*Segall et al.*, 1990].

[13] Postmagmatic structures in Bear Creek include nearly vertical joints and faults [e.g., *Segall and Pollard*, 1983a, 1983b; *Martel et al.*, 1988]. Initial fracturing produced a single set of joints, presumably due to thermal stresses associated with pluton cooling, (Figure 1a) striking predominantly ENE [*Segall and Pollard*, 1983a; *Martel et al.*, 1988; *Bergbauer and Martel*, 1999]. Quartz precipitated in dilatational regions along joints, and subsequent crystal-plastic shearing (>400°C) localized on the joints, producing quartz mylonites (Figures 1b and 1d). This localized crystal plastic shearing of quartz-filled joints marks the initial development of “small faults” [*Martel et al.*, 1988]. As pluton cooling progressed, cataclasis replaced crystal-plasticity as the dominant deformation mechanism [*Griffith et al.*, 2008]. Brittle, cataclastic shear localized on the boundaries between tabular quartz mylonites and host granodiorites (Figures 1b, 1c, and 1e). *Griffith et al.* [2008] showed that some of these brittle slip zones are associated with thin (<300 μm), discontinuous pseudotachylite veins (Figures 1b, 1c, and 1f). The pseudotachylites are typically found in small patches in narrow (<200 μm) slip zones where cataclasis is either poorly developed or completely absent [*Griffith et al.*, 2008]. This observation suggests that pseudotachylite was either not formed in thicker (>200 μm) cataclastic slip zones due to distributed shear (and thus broadened frictional heat generation) or were poorly preserved due to enhanced permeability of the thicker granular cataclasis during exhumation. The presence of pseudotachylite veins along the Bear Creek

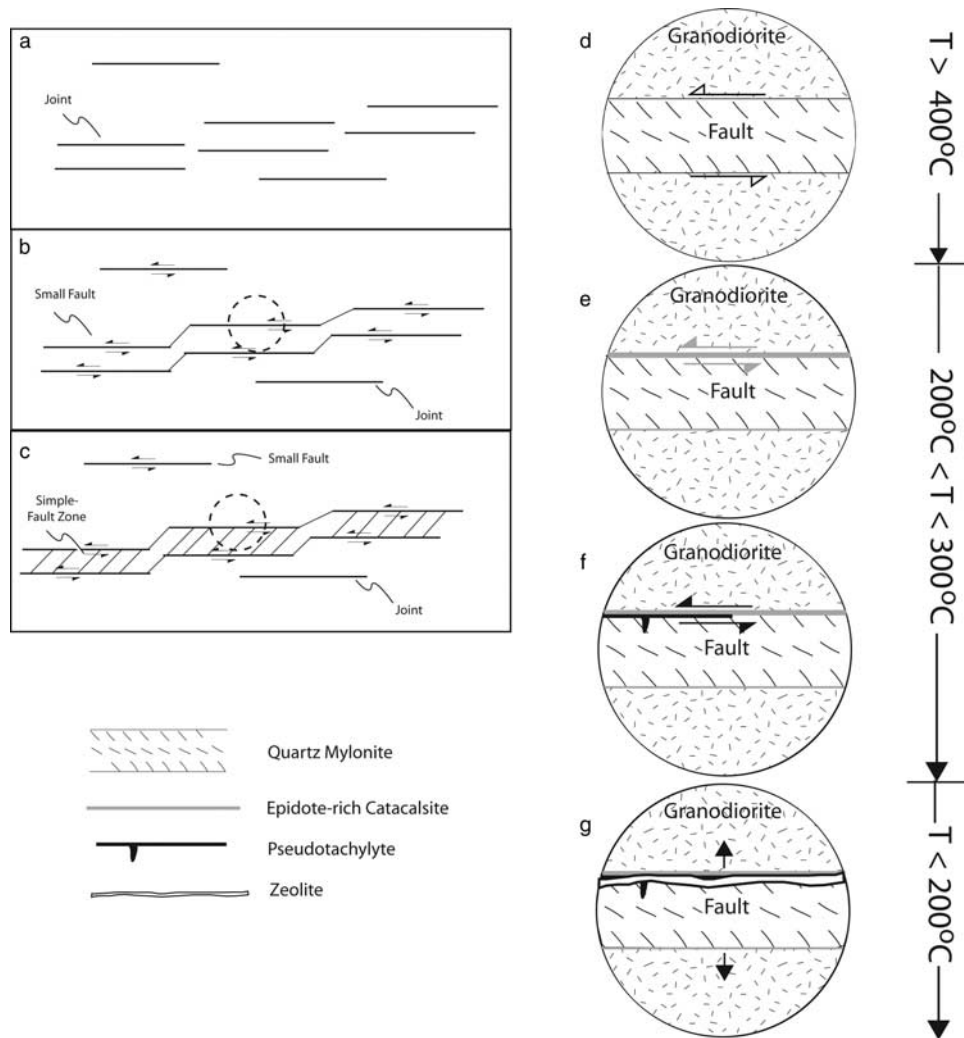


Figure 1. Conceptual model of macroscopic and microscopic evolution of faults in Bear Creek [Griffith *et al.*, 2008]. (a–c) Macroscopic evolution of faults suggested by Martel *et al.* [1988], where in stage I (Figure 1a) joints form in response to thermal stresses; stage II (Figure 1b) is marked by slip nucleation along joints and subsequent linkage to form small faults; and in stage III (Figure 1c) simple fault zones composed of paired small faults linked by secondary fractures form due to interaction of neighboring faults. Martel [1990] also proposed a fourth stage of development in which simple fault zones coalesce to form large, complex fault zones, but the fourth stage has been omitted for simplicity. Dashed circles in Figures 1b and 1c indicate the location of Figures 1d, 1e, 1f, and 1g. (d–g) Microstructural evolution of faults from the time that shearing commences to the transition from shearing deformation to zeolite veining. Figure 1d shows quartz precipitated in dilatational regions along faults is sheared at temperatures greater than 400°C producing quartz mylonites. Figure 1e shows the boundaries between mylonites and granodiorites, which are filled with epidote veins and reactivated by cataclasites cemented by epidote. Locally cataclasites and epidote veins cut across mylonites. Figure 1f shows thin, discontinuous pseudotachylyte veins, which form due to seismic slip, and locally cut mylonites and cataclasites. Figure 1g shows termination of shear deformation, which is signified by opening of faults and zeolite mineralization.

faults suggests that some of these faults were seismic during the brittle phase of their evolution. After the “small fault” stage of development (stage II), simple fault zones (stage III) composed of paired small faults linked by secondary fractures formed due to interaction of neighboring small faults [Martel *et al.*, 1988]. Martel [1990] also proposed a fourth stage of development in which simple fault zones coalesce to form large, complex fault zones. The occurrence of pseudotachylyte has also been reported on the Glacier Lakes fault, a

fault accommodating greater than 100 m of slip, located approximately 50 km south of the Bear Creek faults [Kirkpatrick *et al.*, 2008]. The Glacier Lakes shares many similarities with the Bear Creek faults, including inferred depth of exhumation, host rock type, and microstructure [Kirkpatrick *et al.*, 2008]. In the Martel’s model of fault development the Glacier Lakes fault would be classified as a stage III or stage IV fault zone. Therefore, if the Glacier Lakes fault developed similarly to fault zones of the Bear

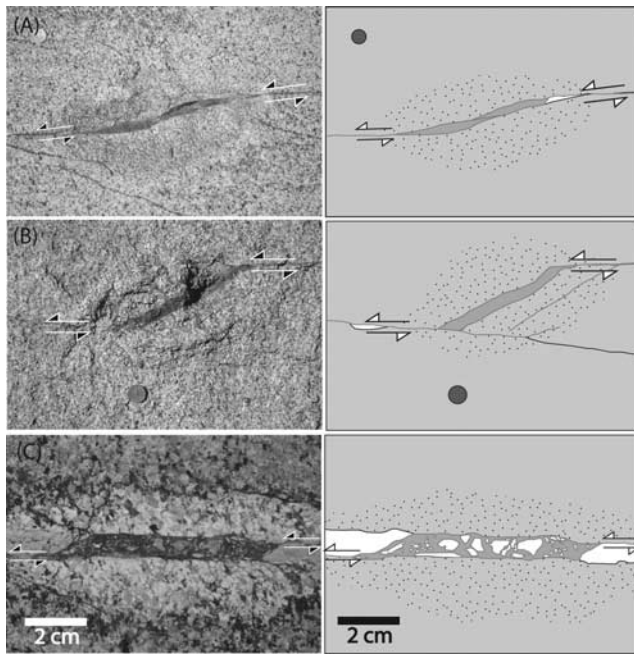


Figure 2. (left) Field photographs and (right) schematic drawings of three different types of epidote-filled dilational jogs found along Bear Creek faults. (a) A releasing bend in a fault. (b) A dilational stepover between two small faults. (c) A dilational stepover between two cataclastic slip surfaces localized on the boundary between tabular quartz mylonites and host granodiorite. The configurations shown in Figures 2b and 2c produce rhomboid-shaped openings (rhombochasms) which can be used as slip markers along the faults. Light gray indicates granodiorite; dark gray indicates epidote; white indicates quartz mylonite; and bleached/speckled indicates altered granodiorite.

Creek area, such as the Gemini fault zone [Martel, 1990; Pachell and Evans, 2002], this would suggest that seismic slip occurred throughout the brittle fault evolution.

3. Rhombochasms

3.1. Field Observations

[14] The Bear Creek small faults are commonly associated with epidote veins in extensional domains along the faults (Figure 2), as for example: (1) at releasing bends along faults (Figure 2a); (2) where two fault segments link in dilational steps (e.g., left step for left-lateral faults; Figure 2b); and (3) at fault tips as extensional splays [Segall and Pollard, 1983a]. A fourth structure, distinctly different from the former three, occurs where the cataclastic slip zone jumps from one side of a quartz mylonite to the other (Figure 2c). In this latter case the veins have a typical rhomboidal shape and are referred to as “rhombochasms” throughout the following sections. Where rhombochasms are present, they are often distributed quasi-periodically (~ 1 rhombochasm per 10–30 cm along strike) along a fault (Figure 3). The rhombochasms and the epidote veins are often associated with bleached halos in the adjacent host rock (Figures 2a–2c), a result of plagioclase and biotite alteration to saussurite and chlorite, respectively. In outcrops orthogonal to faults and parallel to the fault slicken lines (approximately the case in the subhorizontal

Bear Creek outcrops) the length of rhombochasm sides that are parallel to the fault provide a direct estimate of the fault slip during rhombochasm formation (e.g., Figure 3).

[15] Minerals in the rhombochasms are typically uniform in color and texture (prismatic epidote grains with no apparent preferred orientation and minor chlorite). In some cases epidotes are interspersed with brecciated subangular clasts of quartz and the host granodiorite (Figure 2c) resembling implosion breccias [Sibson, 1985, 1986]. The clasts vary in abundance, from random, isolated clasts, to jigsaw-pattered, clast-supported textures similar to that shown in Figure 2c. The matrix in all rhombochasms is dominantly epidote.

3.2. Microstructural Observations

[16] Rhombochasms are filled principally with randomly oriented columnar (~ 0.1 to 2.5 mm in length) epidote and variably with chlorite embedding subangular quartz clasts (Figures 4a–4c). Crystals are not deformed or broken (Figure 4c). Epidote inside the rhombochasm does not show any zoning under polarized light in the optical microscope and in backscattered SEM images. Slip zones (generally < 1 mm thick) entering and departing on the opposite sides of the rhombochasm (Figure 4b) are always left-stepped, switching from the one boundary between quartz vein and host granodiorite to the other, consistent with the left-lateral sense of shear. Rhombochasms along the same fault consistently show the same stepping asymmetry.

[17] In some cases, thin ($< 200 \mu\text{m}$) veins extend partly into the rhombochasms as part of the cataclasite slip zones (Figures 4a and 4d). These veins have some identifying characteristics of pseudotachylite (injection vein, aphanitic, optically cloudy), but upon closer inspection consists of ultrafine-grained epidote. On the interface between the granodiorite and rhombochasm interior, the cataclasite slip zones thin from the slip zone at the mylonite-granodiorite interface toward the distal edge of the rhombochasm. In Figure 4a, these slip zones overlap the rhombochasm by approximately 9 mm along the upper right boundary and approximately 5 mm on the lower left boundary. Thin epidote veins on the upper left and lower right corners of rhombochasms also extend for a short distance (a few centimeters) along the granodiorite-mylonite interface, but these terminate at the rhombochasm opening (Figure 4a). The typical rhombochasm boundary is knife-edged with no cataclasis of the host rock or the minerals in the rhombochasm at the boundary (Figure 4e), whereas slip zones that penetrate into the rhombochasm form a contact between undeformed rhombochasm mineral fillings and the host granodiorite. In some places, slip zones penetrating into rhombochasms can be seen to truncate clasts within the rhombochasm, while these slip zones are truncated at their tips by undeformed epidote crystals (Figure 4f). In other cases the slip zone terminates at the rhombochasm opening (Figure 4g). Unlike faults described by Griffith *et al.* [2008], clasts in the slip zones and the rhombochasms appear to consist exclusively of mineral or rock fragments of the country granodiorite; no clasts of cataclasite have been found either in the rhombochasm or within the cataclastic slip zones.

3.3. Rhombochasm Significance

[18] The rhombochasms can be used to distinguish the contribution of brittle slip and associated cataclasite formation

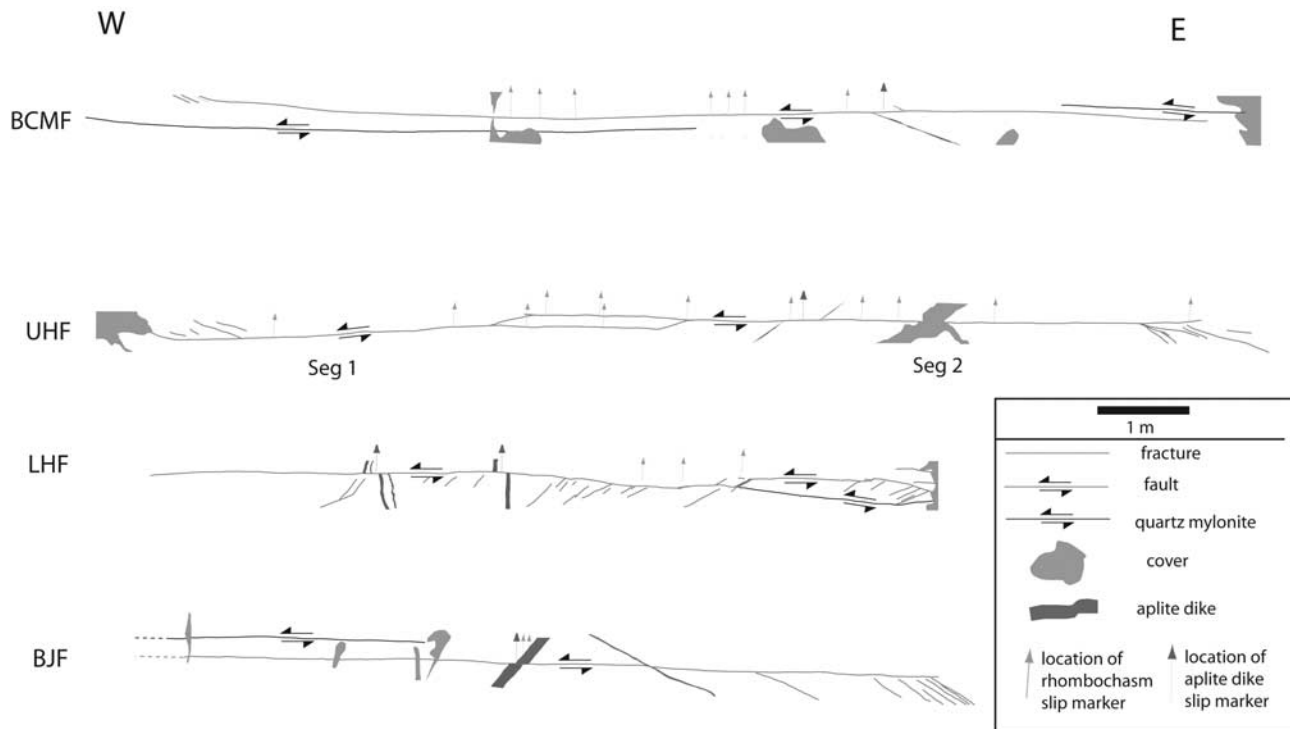


Figure 3. Trace maps of rhombochasm-bearing faults. BCMF, Bear Creek Meadows Fault; UHF, Upper Hilgard Meadows Fault with segments 1 and 2 from Figure 5b; LHF, Lower Hilgard Meadows Fault; BJF, Big Juniper Fault.

to the total observed offset along small faults (as measured by offset of aplite dikes) from the contribution from previous crystal-plastic shearing. The epidote-filled, rhombohedron-shaped dilational jogs opened at bends and stepovers during brittle slip, and are distributed along the length of the faults. We interpret this observation to mean that the length of each rhombochasm approximates the brittle slip magnitude that occurred at the corresponding position along the fault, and we argue that brittle slip occurred along the measured fault lengths in single slip events. The rhombochasm microstructure indicates growth in an open fluid-filled cavity without evidence of incremental growth by the crack-seal mechanism [Ramsay, 1980] (Figure 4a). Epidote crystals are randomly oriented and undeformed within the rhombochasms (Figure 4c). The epidotes were not broken after initial opening and precipitation as should be expected if the rhombochasms opened incrementally, as epidote precipitation occurred after slip ceased on the faults. This interpretation of a single slip episode is supported by the apparent absence of clasts of earlier cataclasite, particularly as cataclasite clasts have been observed as common features in other faults in the Bear Creek drainage.

[19] It is unclear whether or not these events were seismic or aseismic. Some small faults in the Bear Creek area contain pseudotachylytes [Griffith *et al.*, 2008] suggesting that seismic slip occurred during brittle deformation along some faults in Bear Creek. However, as previously noted, pseudotachylytes are only developed (or preserved) locally along small faults and tend to be absent in cataclasite slip zones thicker than $\sim 200 \mu\text{m}$ [Griffith *et al.*, 2008]. Because cataclasites along these faults are consistently thicker than $200 \mu\text{m}$ (Figure 4g), we should not expect to see pseudota-

chylyte if the previous observations are predictive. However, pseudotachylytes described by Griffith *et al.* [2008] do show common static overgrowths of epidote. This suggests that the rhombochasm-bearing small faults investigated in this study developed during the same ambient conditions as the pseudotachylyte-bearing faults. Implosion-like breccias in some rhombochasms also point toward a fast rate of deformation, as these breccias have been interpreted to form by implosion or collapse in response instantaneous, sharp fluid pressure gradients introduced by rapid opening of a void [e.g., Sibson, 1986].

[20] Slickenlines on faults commonly plunge less than 15° on the studied faults, and less than 20° on most faults exposed in Bear Creek [e.g., Martel *et al.*, 1988; Griffith *et al.*, 2008]. Therefore offset measured from the rhombohedron lengths on subhorizontal outcrop should underestimate the actual slip by at most 4% (error = $1 - \cos 15^\circ$). The unique combination of factors listed above distinguishes these observations from previous attempts to estimate coseismic parameters such as stress drop from exhumed faults because we can constrain both the rupture length and slip [e.g., Sibson, 1975; Di Toro *et al.*, 2005].

3.4. Slip Distributions

[21] Figure 3 shows the profiles of four small faults in the Bear Creek area exposed along their entire lengths, ranging from 8 to 12 m. We measured the total slip (from aplite dike offset) and the distributions of rhombochasm lengths for two faults, the Bear Creek Meadows Fault (BCMF) and the Upper Hilgard Fault (UHF) (Figure 5).

[22] The BCMF consist of an en echelon array of highly overlapping, right-stepping fault segments. We estimated

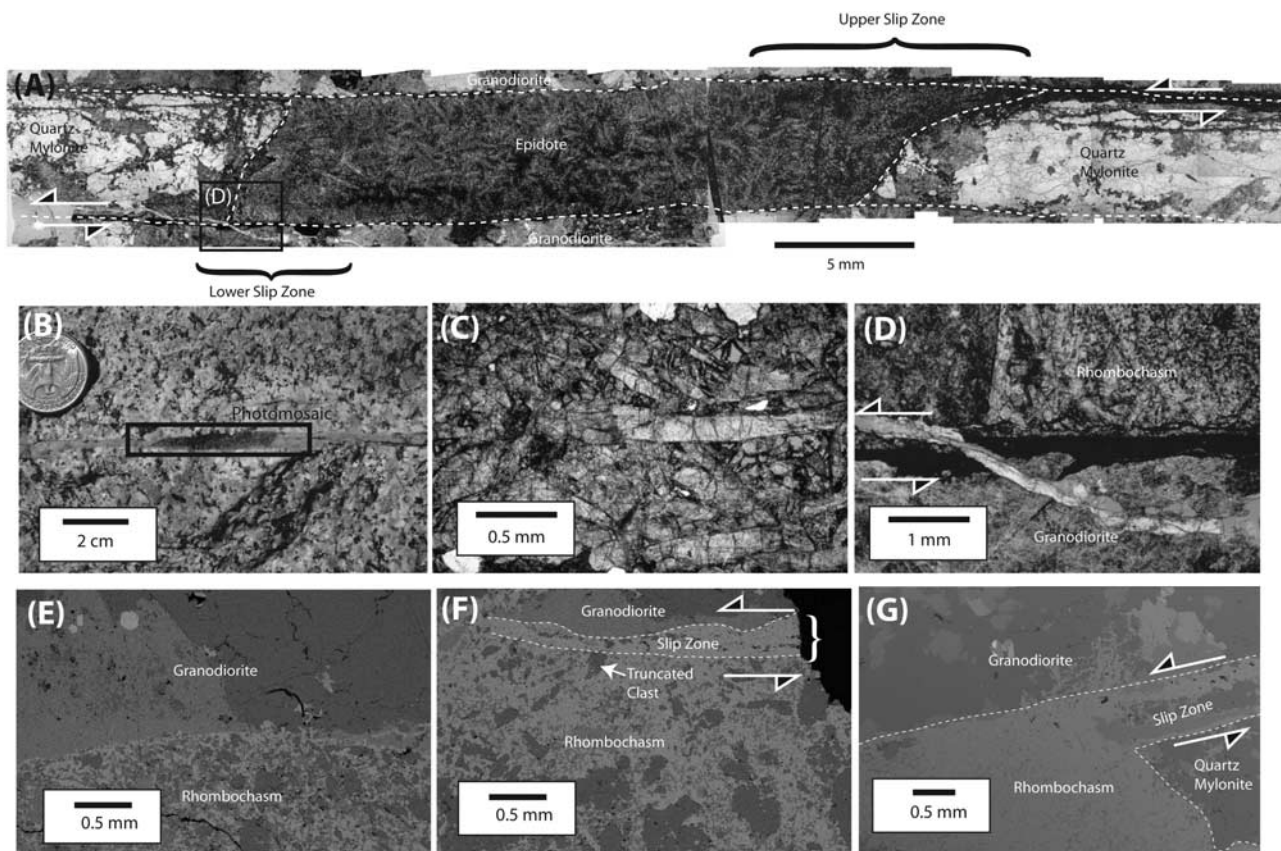


Figure 4. Rhombochasm microstructures. (a) Photomosaic of a rhombochasm on the Bear Creek Meadows Fault (Figure 3, BCMF) (optical photomicrograph, plane polarized light). (b) Field photograph of rhombochasm pictured in Figure 4a. (c) Epidote crystals and quartz grains from Lower Hilgard Meadows Fault (Figure 3, LHF) (optical photomicrograph, plane polarized light). (d) Dark vein penetrating into the rhombochasm from BCMF (see Figure 4g). This vein is part of the slip zone extending into the rhombochasm and has some identifying characteristics of pseudotachylyte (injection vein, aphanitic, optically cloudy), but upon closer inspection consists of ultrafine-grained epidote. The dark vein is truncated by a later white zeolite-bearing vein (optical photomicrograph, plane polarized light). (e) Contact between rhombochasm filling and granodiorite. No evidence of slip is preserved along this contact (SEM backscattered electron image). (f) The $\sim 0.2\text{--}0.4$ mm thick slip zone separating rhombochasm filling and granodiorite (SEM backscattered electron image). Figures 4e and 4f were taken along the same rhombochasm-granodiorite contact from fault BCM. (g) Slip zone along the BCMF which does not penetrate into the rhombochasm. Image is taken from a rhombochasm several centimeters from the rhombochasm from Figures 4e and 4f along the BCMF.

brittle slip using seven rhombochasms distributed along the central segment (Figure 3, BCMF). No hard linkage was observed along the overlapping echelon segments on BCMF, nor was any macroscopic evidence for brittle reactivation of the mylonite fracture fillings on the segments overlapping the central one. The zero slip data points on either side of each slip distribution (Figure 5) correspond to the tips of the central fault segment. Rhombochasms occur within the data gaps (e.g., position ranges 590–770 cm and 930–1350 cm), but they were too complicated in shape to use as slip markers. The presence of rhombochasms along the length of the BCMF does indicate that brittle slip occurred along the entire length of the fault segment; therefore the measured length of the fault segment accurately represents the source dimension. The slip maximum occurs slightly west of center and appears to taper toward the fault tips. The average measured brittle slip

on the fault is 2.1 cm. This average measured slip value is consistent with estimates of coseismic slip on pseudotachylyte-bearing small faults in Bear Creek [Griffith *et al.*, 2008].

[23] The UHF (Figure 3b) consists of two hard-linked fault segments (i.e., the fault segments are linked by fractures across the relay zone). In the case of the UHF, only the easternmost fault tip of segment 2 is exposed. The westernmost fault tip of segment 1 is buried under debris. This debris cover is approximately 2–3 m wide, and the fault does not continue on the other side. Near the debris cover, splay cracks are concentrated on the southern side of the fault. These two observations suggest that the fault length is no more than a couple of meters greater than the visible length. Rhombochasms are distributed more evenly than in the BCMF; therefore the slip distribution is more clearly discernable (Figure 5b). The slip distribution appears to be flat along most

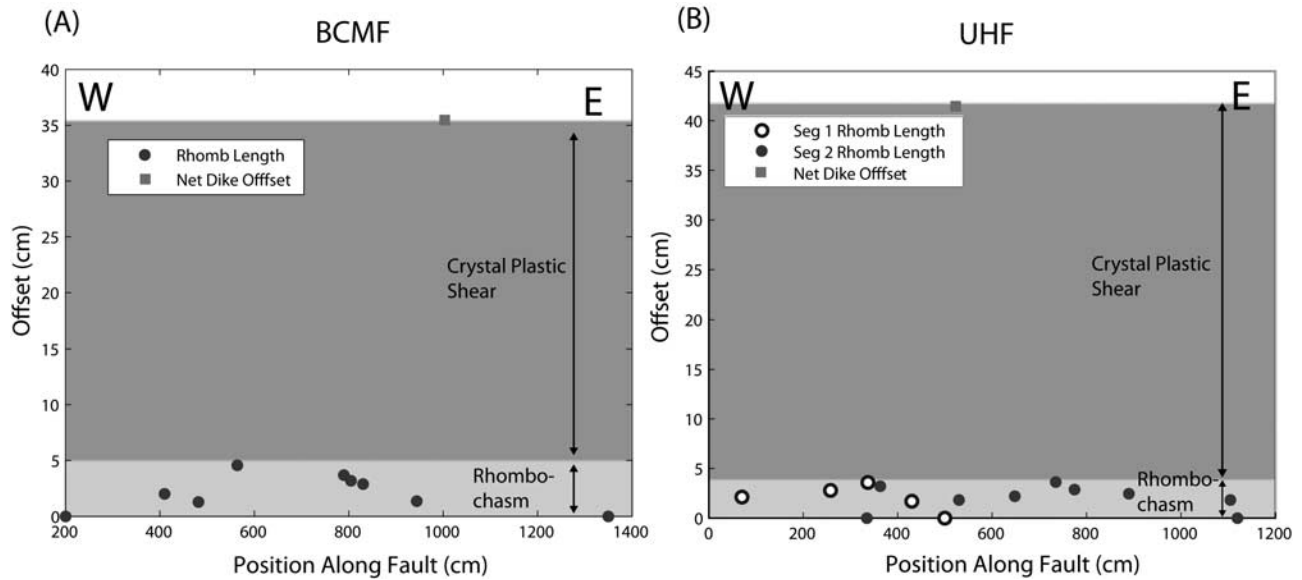


Figure 5. Slip distributions along (a) the Bear Creek Meadows Fault (BCMF) and (b) the Upper Hilgard Fault (UHF), as determined by measuring the length of rhombochasms (brittle, cataclastic shear) and dike offset (crystal plastic shear + brittle, cataclastic shear).

of the fault and tapers sharply at the western end. Slip tapers more gently on each segment in the relay zone. The average measured brittle slip on the UHF is 2.0 cm.

[24] The systematic variance of rhombochasm lengths (Figure 5), with a maximum length near the fault center and tapering toward the ends, also supports the interpretation that all of the rhombochasms formed at the same time, rather than in isolated patches. As suggested previously, the rhombochasm length distribution measured from outcrop maps should closely approximate the brittle slip distribution, and possibly the seismic slip distribution, along these faults.

[25] Also, the slip calculated from rhombochasm lengths provides some insight into the relative contribution of different deformation mechanism to total fault offset during the longer term fault evolution. The observed offset of an aplite dike on the BCMF is approximately 35 cm, while that measured along the UHF is 42 cm. Both of these are significantly greater than the measured brittle slips. This gives us an indirect way to estimate the ductile (i.e., crystal-plastic shear of quartz) contribution to slip. The discrepancy between brittle, cataclastic slip and total offset should approximate the offset due to crystal-plastic shearing of the tabular quartz mylonites extending much of the length of the faults. A direct measure of the plastic shear preceding brittle slip is not possible in the studied faults given the very heterogeneous deformation of the quartz veins with the domains of dynamically recrystallized quartz forming an irregular foliation surrounding domains of weakly deformed quartz vein fabric. However, the presence of a dominant contribution of plastic deformation to the total slip is indicated by the strong slip gradients along the fault (e.g., slip drops to zero from 35 cm in about 2 m along the BCMF) which are not consistent with a purely elastic deformation of the host granodiorite but are typical of the high temperature deformation [Christiansen and Pollard, 1997; Pennacchioni, 2005].

3.5. Stress Drop

[26] The constant stress drop model used to calculate the stress drops of ruptures on the rhombochasm-bearing Bear Creek faults and in many seismological models [e.g., Kanamori and Anderson, 1975] is a special case of the Eshelby [1957] analytical solution for the elastic field of an ellipsoidal inclusion. The circular “penny-shaped crack” model assumes that the principal ellipsoidal axis c is much smaller than the other principal axes, a and b (Figure 6). If the elliptical fault can be approximated as a circle ($a = b$) the slip distribution is given by [Eshelby, 1957, equation (5.7)]:

$$\pm D(r) = \frac{\Delta\sigma}{\mu} \frac{4(1-\nu)}{\pi(2-\nu)} R \sqrt{1 - \frac{r^2}{R^2}} = \frac{1}{2} \Delta D(r) \quad (1)$$

where D is the particle displacement on either side of the fault and ΔD is the displacement discontinuity (slip) across the fault at each point r , $\Delta\sigma$ is the stress drop, μ is the elastic shear modulus of the medium, and ν is the Poisson ratio. The model assumes a constant stress drop on a circular fault of radius R in a linear elastic whole space. The expression for $\Delta\sigma$ of an earthquake given the average slip $\Delta\bar{D}$ across the fault and assuming a Poisson solid ($\nu = 0.25$) is [e.g., Keilis-Borok, 1959; Kanamori and Anderson, 1975]:

$$\Delta\sigma = \frac{7\pi}{16} \mu \frac{\Delta\bar{D}}{R}. \quad (2)$$

The assumption of a Poisson solid is a good approximation for granodiorite based on laboratory tests [Gerçek, 2007]. Using this relationship, a shear modulus of $\mu = 30$ GPa, average slip $\Delta\bar{D} \approx 2.1$ cm, and radius $R = 5.75$ m (Table 1) the coseismic static stress drop on the BCMF is approximately $\Delta\sigma \approx 150$ MPa. A similar calculation based on the UHF yields a stress drop of 130 MPa. These are large stress

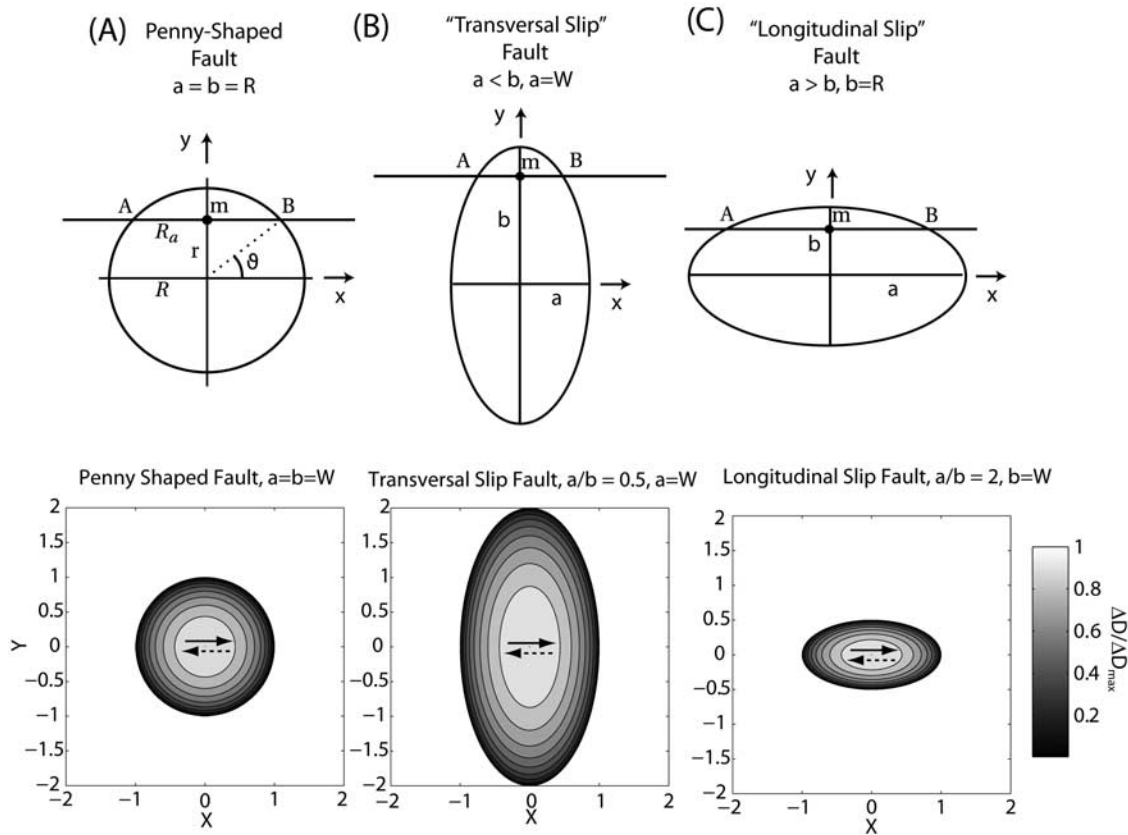


Figure 6. Constant stress drop models for elliptical faults with aspect ratios (a/b) varying from 0.5 to 2. For each model, the upper diagram shows the coordinate system and the hypothetical erosional surface exposed in outcrop is shown by the line A–B. The lower plot in each diagram shows predicted slip distributions for a given constant stress drop. Note that the horizontal axis a is equal in all plots. Only the unknown b axis varies in each plot. (a) Penny shaped-crack model ($a/b = 1$). (b) Transversal slip fault ($a < b$). (c) Longitudinal slip fault ($a > b$). See text for more detail.

drop values relative to the expected range 0.1 to 100 MPa. Before we discuss the implications of these findings, we first analyze potential sources of error in the analysis.

4. Discussion

4.1. Uncertainty and Analysis Limitations

[27] Here we identify and attempt to quantify the sources of error for the stress drops calculated in section 3. Possible sources of error are divided into three groups: (1) assumption of the source geometry, (2) differentiation between seismic and aseismic slip, and (3) measurement of slip. The calculated stress drops for the BCMF and the UHF are summarized in Table 1.

4.1.1. Source Geometry

[28] Eshelby's general solution for slip on an elliptical crack with aspect ratio a/b on which slip is parallel to the a axis is given by:

$$\pm D(x, y) = \frac{b \Delta \sigma}{C_1 \mu} \sqrt{1 - \frac{x^2}{a^2} - \frac{y^2}{b^2}} = \frac{1}{2} \Delta D(x, y) \quad (3)$$

This is the more general form of equation (1) in Cartesian coordinates where slip is parallel to the x -axis. The coefficient

C_1 is a function of the aspect ratio of the elliptical fault geometry and is given by *Eshelby* [1957, equation 5.3]:

$$C_1 = E(k) + \frac{\nu}{1-\nu} \frac{K(k) - E(k)}{k^2}; \quad a > b, k = \sqrt{1 - b^2/a^2}$$

$$= \frac{b}{a} \left[E(k) + \frac{\nu}{1-\nu} \frac{K(k) - a^2/b^2 E(k)}{k^2} \right]; \quad b > a, k = \sqrt{1 - a^2/b^2}$$

$$= \frac{\pi(2-\nu)}{4(1-\nu)}; \quad a = b \quad (4)$$

Here $E(k)$ and $K(k)$ are complete elliptical integrals of the first and second kind respectively. *Madariaga* [1977] evaluated

Table 1. Summary of Fault Source Parameters

Fault	W (m)	a/b	ΔD_{ave} (cm)	ΔD_{max} (cm)	Dike Offset (cm)	$\Delta \sigma$ (MPa)
BCMF	5.75	1	0.8–2.1	4.5	35	150
BCMF	5.75	0.5	0.8–2.1	4.5	35	110
BCMF	2.88	2	0.8–2.1	4.5	35	250
UHF	6.25	1	0.8–2.0	3.6	42	130
UHF	6.25	0.5	0.8–2.0	3.6	42	90
UHF	3.13	2	0.8–2.0	3.6	42	220
LHF	-	-	2.6	5.1	14	-
BJF	-	-	1.2	2.6	4.8	-

similar expressions for the stress drop in terms of the *average* slip, $\Delta\bar{D}$:

$$\Delta\sigma = \frac{\mu}{C_2} \frac{\Delta\bar{D}}{W} \quad (5)$$

where W is the shortest principal axis of the fault model (i.e., $W = R$ for the circular fault). For the circular (“penny-shaped”) fault the commonly cited result for the coefficient C_2 is $16/7\pi$ [e.g., *Kanamori and Anderson, 1975*]. C_2 can be calculated for elliptical model faults of a variety of aspect ratios using [*Madariaga, 1977*]:

$$\begin{aligned} C_2 &= 4 \left[3E(k) + \frac{K(k) - b^2/a^2 E(k)}{k^2} \right]^{-1}; \quad a > b, k = \sqrt{1 - b^2/a^2} \\ &= 4 \left[3E(k) + \frac{a^2 K(k) - E(k)}{b^2} \right]^{-1}; \quad b > a, k = \sqrt{1 - a^2/b^2} \end{aligned} \quad (6)$$

In calculating the stress drop, we previously made the simplifying assumptions that (1) the fault mapped in two dimensions with measured half-length R_a can be represented in three dimension by a circular fault; and (2) that the radius R of the fault is equivalent to the measured half-length R_a . Below we assess the net effect of each of these assumptions.

[29] First, we keep the assumption that the fault is circular, but we relax the assumption that the apparent radius R_a exposed at the Earth’s surface is equal to the actual radius R of the crack. Let the line A–B (Figure 6a) be the intersection of the circular fault with the Earth’s surface. Because the slip maximum according to equation (1) occurs at the center of the fault ($r = R$), the stress drop can be expressed as a function of the maximum slip, ΔD_{\max} :

$$\Delta\sigma = C_1 \mu \frac{\Delta D_{\max}}{R} \quad (7)$$

With no knowledge of the actual fault size, using the apparent radius R_a and the maximum apparent slip D_a measured at point m , an apparent stress drop $\Delta\sigma_a$ is obtained:

$$\Delta\sigma_a = C_1 \mu \frac{\Delta D_a}{R_a} \quad (8)$$

However, according to Figure 6a we may replace $r = R \sin \theta$ in equation (1) to obtain:

$$D(r) = \frac{\Delta\sigma}{C_1 \mu} R \sqrt{1 - \sin^2 \theta} \quad (9)$$

and using the fact that $R_a = R \cos \theta$ we obtain:

$$\Delta\sigma_a = \frac{\Delta\sigma \sqrt{1 - \sin^2 \theta}}{\cos \theta} = \Delta\sigma. \quad (10)$$

In conclusion, the ratio D_a/R_a remains identical to D/R ; as a consequence, measurement of apparent maximum slip and radius along any arbitrary section of a circular model fault yields the correct stress drop estimate through equation (3). The same observations apply when using average apparent

slip, instead of the maximum apparent slip: the correct scaling with stress drop is maintained through any section of the model fault. It can also be shown that the apparent half-length, a , of any elliptical fault scales linearly with slip.

[30] If the assumption that the crack is circular is dropped, and the possibility is considered that the fault may approximate an ellipse, the resulting stress drop will vary depending on the aspect ratio of the fault and the length of the semiminor axis. We can calculate the stress drop for elliptical faults using equations (5) and (6). If we assume that a reasonable range of elliptical fault aspect ratios is in the range $0.5 \leq a/b \leq 2$, then we can calculate the range of possible stress drops represented by two-dimensional fault exposures. Faults of aspect ratios less than one, on which the slip direction is parallel to the semiminor axis (Figure 6b), were called “transversal slip” faults by *Madariaga* [1977] while faults with aspect ratios greater than one, on which slip is parallel to the semimajor axis, were classified as “longitudinal slip” faults (Figure 6c). If the BCMF is a transversal slip fault with an aspect ratio equal to 0.5, the corresponding stress drop is reduced to $\Delta\sigma \approx 110$ MPa. Assuming the BCMF is a longitudinal slip fault with an aspect ratio equal to 2 implies that the semiminor axis is vertical, and the apparent length of the semiminor axis is half the measured length of the fault in the field. Correspondingly, using the value $W = b = 3$ m, and the appropriate expression from equation (6), the corresponding stress drop is $\Delta\sigma \approx 250$ MPa. Thus, taking into account the geometric error introduced by extrapolating the two-dimensional map to three dimensions extends the range of possible stress drop values to $110 \text{ MPa} \leq \Delta\sigma \leq 250 \text{ MPa}$. Similar estimates for the stress drop on the UHF yield stress drops of $90 \text{ MPa} \leq \Delta\sigma \leq 230 \text{ MPa}$. Extending this analysis to fault aspect ratios outside the range $0.5 \leq a/b \leq 2$ changes the calculated stress drops very little from the range in stress drop estimates presented here.

4.1.2. Differentiation Between Seismic and Aseismic Slip

[31] Ultimately, stress drop and slip under brittle conditions should not be very different whether they occurred quasi-statically or seismically [*Madariaga, 1976*]. Owing to dynamic overshoot, slip (and stress drop) may be as much as 30% larger during seismic slip [*Madariaga, 1976*]. The recognition of seismic slip from outcrop observations along faults remains a difficult and controversial topic [e.g., *Cowan, 1999*]. Several lines of evidence suggest that slip may have been seismic. First, the microstructures within the opening rhombochasms suggest that the associated slip was nearly instantaneous. These microstructures include randomly oriented epidote grains in all rhombochasms as well as implosion breccias. The fact that these microstructures show no postformation shearing disruption suggests that all of the rhombochasms formed in a single event. Similar crack-infilling structures in samples from the Nojima fault have been interpreted as having been related to coseismic fluid circulation [*Boullier et al., 2004*]. Second, thin (<1 mm) pseudotachylyte veins are found on nearby Bear Creek faults [*Griffith et al., 2008*]. The magnitude of coseismic slip inferred for these pseudotachylyte bearing faults (1–7 cm) is consistent with the average brittle offset estimated for the rhombochasm-bearing faults. Last, pseudotachylytes have been found along wavy faults at contractional bends whereas epidote filled rhombic openings are found at extensional

bends along the same fault [e.g., *Kirkpatrick and Shipton, 2008*]. Therefore, seismic slip appears to have been associated with opening of voids and subsequent mineralization. It should be noted that pseudotachylytes described by *Griffith et al. [2008]* were either not formed or not preserved wherever significant epidote mineralization and associated alteration were present, and as already noted, the pseudotachylytes were associated either with no cataclasite or cataclasites thinner than 200 μm ; therefore the lack of pseudotachylyte along the rhombochasm-bearing faults, which show abundant evidence for fluid saturation and are consistently thicker than 200 μm certainly does not preclude seismic slip on the faults described in the present study. These observations are consistent with an interpretation that brittle slip along these faults was seismic; however, they do not constitute conclusive proof of seismic slip.

4.1.3. Measurement of Slip

[32] We present a kinematic model for the rhombochasm formation (Figure 7) to justify in more detail our assumption that the length of the rhombochasm represents the magnitude of slip in a single event. The faulting begins on a tabular quartz mylonite, bounded on either side by granodiorite, with crystal-plastic shearing across its ~ 1 cm thickness and bounded on either side by granodiorite (Figure 7a). Shearing across the quartz mylonite involves no displacement discontinuity at the mylonite-granodiorite interfaces. Subsequently, more localized brittle shearing (slip) develops across <1 mm thickness the interfaces forming cataclasite slip zones in a left stepping configuration (Figure 7b). A small amount of localized shearing continues until the tensile strength of the quartz mylonite in the relay zone is exceeded [e.g., *Segall and Pollard, 1980; Martel and Pollard, 1989; Mutlu and Pollard, 2008*], and a tensile opening fracture forms, linking the two cataclastic slip zones (Figure 7c). This linking fracture cuts the cataclastic zones into short abandoned, nonshearing zones including the tips, and actively shearing echelon zones on either side of the tabular quartz mylonite. As slip progresses in the echelon cataclastic zones, deformation in the quartz mylonite is primarily ascribed to opening of the rhombochasm (Figure 7d). On the interface between the granodiorite and rhombochasm interior, because there is no new cataclasite generation, the cataclasite thins from the actively slipping zone toward the distal edge of the rhombochasm. As shearing ceases, within the rhombochasm only the remnants of the cataclasite closest to the actively shearing cataclasite zone, if any at all, are preserved (Figure 7e). Epidote is subsequently precipitated and fills the rhombochasm with euhedral, randomly oriented crystals (Figure 7f). In this model, the length of the rhombochasm should approximate the magnitude of slip, ΔD , of a single slipping event as well as the magnitude of the total brittle slip on the fault.

[33] We note that a small amount of underestimation of slip is introduced by the assumption that this process can be approximated by the kinematic block model summarized above. In Figure 7c, a small amount of shearing must accumulate along the cataclastic zones before the tensile strength in the relay zone is exceeded [e.g., *Segall and Pollard, 1980*]. This shearing is not necessarily recorded by the rhombochasm opening; however, we expect the amount of shearing necessary to breach the relay zone to be very small relative to the rhombochasm length as the tensile strength of

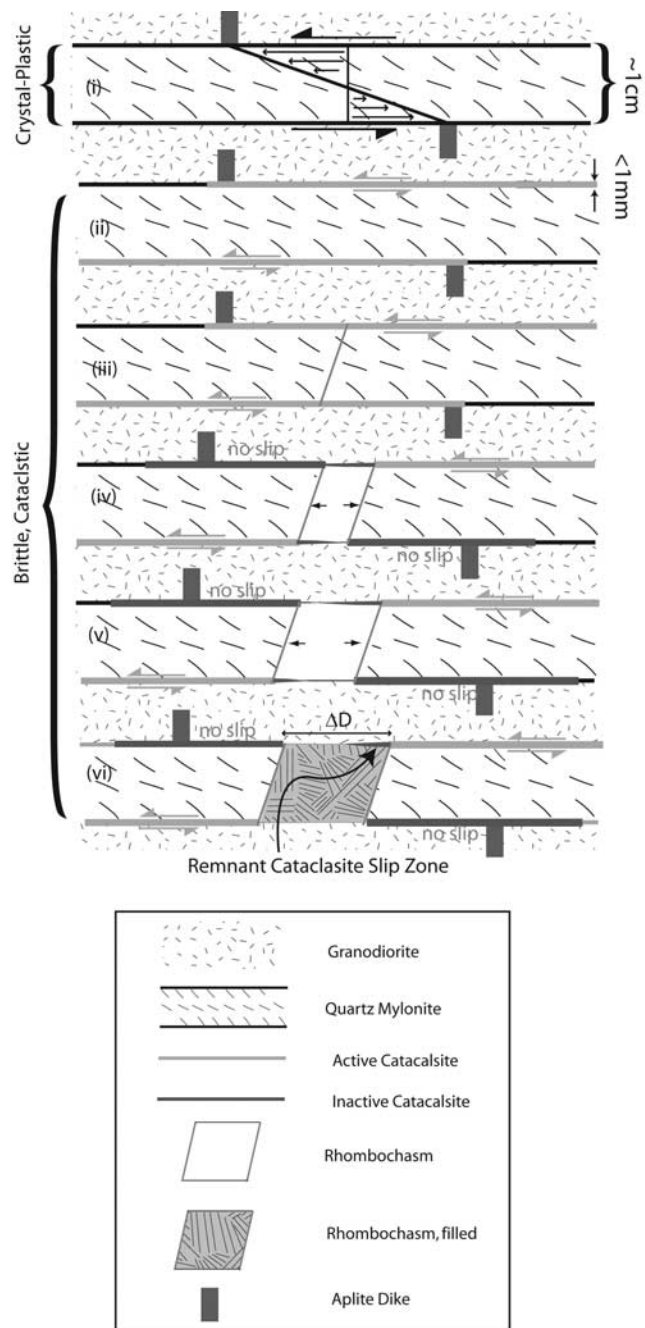


Figure 7. Kinematic model for rhombochasm formation showing (a) the initial, crystal-plastic shearing, (b) the initiation of brittle, cataclastic shear, and (c–f) the steps of rhombochasm initiation, opening, cease, and mineral precipitation. Note that the dark gray aplite dikes illustrate the relative offset across the fault associated with each stage. See text for complete discussion.

quartz mylonite between the cataclasite slip zones should be exceeded with net relative displacement across the fault on the order of 1 mm or less. The average rhombochasm length measured on the Bear Creek faults is approximately 2 cm, within the range of single slip values estimated for nearby pseudotachylyte-bearing faults based on conductive heat transfer calculations [*Griffith et al., 2008*].

[34] What may have significant implications for the calculated stress drop is the assumption that the measured opening was associated with purely elastic deformation in the surrounding granodiorite. It is clear from the microstructural observations that the rhombochasms were not disrupted after mineralization. However, it is difficult to constrain the period of time between opening and complete mineralization (i.e., how long the epidote took to grow, between the stages shown in Figure 7e and 7f). Solely on the basis of microstructural observations of the rhombochasms, we cannot rule out the possibility that some portion of the fault offset recorded by rhombochasm length was seismic, and the remaining offset accumulated by transient creep after the dynamic event before mineralization took place. For example, if we idealize the granodiorite as a linear viscoelastic Maxwell material [Flügge, 1967] in which slip is driven by constant remote shear stress, the average shear strain near the fault is the sum of the elastic and viscous strain. Under this scenario, the stress drop could be significantly less than our estimates. If the viscous strain was significant relative to the elastic strain, some evidence of inelastic off-fault deformation in the form of ductile deformation mechanisms should be apparent. Segall and Simpson [1986] and Bürgmann and Pollard [1992] have described mylonitic fabric development in granodiorites around small faults in the Bear Creek area. These fabrics are particularly well developed in contractional steps between faults [Bürgmann and Pollard, 1992]; however, these mylonitic foliations are defined by dynamic recrystallization of biotite, plagioclase, and quartz [Griffith et al., 2008]. These deformation mechanisms are expected to occur at temperatures greater than 400°C and are thus not expected to occur concurrently with brittle shearing on the small faults. We have observed pressure solution and bulging recrystallization within quartz mylonites and quartz grains that overprint higher grade fabrics; however, it remains unclear how much deformation was accommodated by these mechanisms. While these lower-grade deformation mechanisms are not as prevalent as the higher-grade mylonitic fabrics, a more detailed systematic study of low grade off-fault ductile deformation mechanisms would need to be conducted to assess the viscous contribution to the slip measured along the faults. On the basis of the apparent paucity of microstructural observations of crystal-plastic or viscous mechanisms, we lean toward the interpretation that the rhombochasm length represents a single-jerk fault offset.

[35] Another limitation of our analysis arises from the fact that the slip distributions shown in Figure 5 are nonelliptical. This indicates that the uniform stress drop model is not sufficient to explain the observations. Bürgmann et al. [1994] showed that nonelliptical earthquake slip distributions may be explained by: (1) changes in frictional strength along faults; (2) spatial gradients in the stress field; (3) inelastic deformation near fault terminations; (4) variations of the elastic moduli of the host rocks; and (5) fault interaction. For example, the slip distribution on the BCMF reaches a maximum near the center of the fault and tapers to the fault tips. One explanation is the interaction with overlapping segments, i.e., mechanism 5. If this is the case, and those segments also slipped in a simultaneous event, the actual stress drop could be smaller than calculated here. On the other hand, the slip distribution measured along the UHF is flat

along the majority of the fault and appears to taper sharply at the ends. This fault was isolated from nearby faults by a distance roughly equivalent to the fault trace length, so significant interaction was unlikely. The nonelliptical slip distribution on the UHF could result from mechanisms 1 or 3 mentioned above. Bürgmann et al. [1994] showed that one can fit various nonelliptical models to the data and evaluate the nonuniform stress drop. Applying this approach to the Bear Creek faults could yield interesting insights into the connection between nonelliptical slip distributions and the mechanisms listed above and should be an area of future study. Nonelliptical slip distributions are common where they have been measured precisely [e.g., Walsh and Watterson, 1988; Cowie and Shipton, 1998; Maerten et al., 1999; Maerten and Pollard, 2001; Manighetti et al., 2001; Manighetti et al., 2005], and the Bear Creek faults are no exceptions. However, for the present study the use of a constant stress model is sufficient for a first-order estimate of the static stress drop associated with these ancient slip events. Because it is an assumption made in most seismological studies of small earthquakes, this assumption also makes our estimate directly comparable to seismological estimates.

4.2. Stress Drop Implications

[36] Stress drops calculated using values from field mapping of the BCMF and UHF are in the range $90 \text{ MPa} \leq \Delta\sigma \leq 250 \text{ MPa}$ considering a range of three-dimensional source geometries. These values are near the upper bound of scaling relationships based on the bulk of seismological data available [Kanamori, 1994; Abercrombie, 1995], they are not without precedent. Stress drops on the order of hundreds of MPa appear to be rare but have been observed using seismology [Kanamori, 1994]. Munguia and Brune [1984] calculated stress drops in excess of 200 MPa for events in the Victoria, Baja California earthquake swarm of 1978. Kanamori et al. [1990, 1993] estimated stress drops for a small earthquake in Pasadena (California) between 30 and 200 MPa. Imanishi and Ellsworth [2006] studied 34 M-0.2-M2.1 earthquakes near Parkfield (California) from the SAFOD Pilot Hole Array and found that half had stress drops greater than 10 MPa, with some exceeding 50 MPa. Nadeau and Johnson [1998] estimated stress drops on the order of 100 MPa and greater for repeating microearthquakes near Parkfield. They found that stress drops increased with decreasing seismic moment up to $\Delta\sigma \approx 2000 \text{ MPa}$ for the smallest earthquakes ($W \approx 0.5 \text{ m}$) [Nadeau and Johnson, 1998]. This is approximately the lattice shear strength of an asperity in granitoid rocks with no unhealed flaws [Sammis et al., 1999]; therefore they may significantly overestimate the actual stress drops associated with repeating earthquakes.

[37] This would imply that the Bear Creek faults were “strong” faults as defined by Kanamori [1994]. The interpretation that the Bear Creek faults represent “strong” faults is consistent with interpretations regarding observations of pseudotachylite-bearing faults in other locations [e.g., Di Toro and Pennacchioni, 2005; Sibson and Toy, 2006]. Our observations indicate that the stress drop associated with earthquake ruptures along these faults represent a large percentage of total fault strength.

[38] Although caution should be used in extrapolating the results from a very small and local number of samples, we may attempt a speculative generalization regarding the

broader implications of this study. The result that stress drop is relatively high on the observed faults, as compared to the average stress drop generally assumed on seismic faults may be either (1) because the Bear Creek faults happened to be at the large end of the stress drop range owing to a specific geologic or tectonic property only or (2) because small faults like those observed here have in general larger stress drops; hence self-similarity is not verified at all scales.

[39] One potential justification for argument (1) may lie in the nature of the interface on which the slip events occurred. All of the brittle slip that took place on the rhombochasm-bearing faults occurred on the interface between mylonitized quartz veins and the adjacent host granodiorite. This interface may have represented an at least partially healed asperity, stronger than a typical frictional fault, yet weaker than the surrounding undamaged granodiorite such that flaws concentrated and grew along the quartz mylonite-granodiorite interface.

[40] If argument 2 is correct this may imply that faults are highly inhomogeneous and large earthquakes are composed by a sum of small asperities with large stress drop within an average fault surface with small stress drop [e.g., Bouchon, 1997]. This might suggest that stress drops during small earthquakes, constituted by single asperities, would be relatively high. Argument 2 would also explain the similarity with Parkfield earthquakes (and other data from small earthquakes) without necessarily invoking a geological coincidence. Consistent with this line of thinking, results of laboratory failure experiments also might be seen as indicative only of locally large stress release at asperities during natural earthquakes.

5. Conclusions

[41] Using detailed mapping of small faults in the Bear Creek drainage of the central Sierra Nevada, we estimate coseismic stress drops for ancient earthquakes using rhombochasms as slip markers. This method constrains, with high resolution in two dimensions, the source dimensions of ancient brittle slip events. Errors introduced in the stress drop calculations by inferring the three-dimensional fault geometry from the mapped geometry is approximately a factor of two. The total range of possible stress drops is $90 \text{ MPa} \leq \Delta\sigma \leq 250 \text{ MPa}$. This is larger than typical estimates for small earthquakes and at the upper limit of self-similar scaling laws for all earthquakes. Therefore we suggest that faults of the Bear Creek area were strong faults, and earthquakes along these faults represented static stress drops that were a large fraction of the total fault strength.

[42] **Acknowledgments.** The authors would like to thank A.-M. Boullier, J. D. Kirkpatrick, and associate editor E. Brodsky for constructive reviews of this manuscript. Suggestions by P. Segall and M. Zoback also greatly improved the manuscript. This work was supported financially by the Rock Fracture Project at Stanford, the Fondazione Cassa di Risparmio di Padova e Rovigo ("progetti di Eccellenza") in Padova, and the USEMS European Research Council Starting Grant project.

References

Abercrombie, R. E. (1995), Earthquake source scaling relationships from -1 to 5 ML using seismograms recorded at 2.5-km depth, *J. Geophys. Res.*, **100**, 24,015–24,036, doi:10.1029/95JB02397.

Ague, J. J., and G. H. Brimhall (1988), Magmatic arc aysymmetry and distribution of anomalous plutonic belts in the batholiths of California: Effects of assimilation, crustal thickness, and depth of crystallization,

Geol. Soc. Am. Bull., **100**, 912–927, doi:10.1130/0016-7606(1988)100<0912:MAADO>2.3.CO;2.

Aki, K. (1967), Scaling law of seismic spectrum, *J. Geophys. Res.*, **72**, 1217–1231, doi:10.1029/JZ072i004p01217.

Archuleta, R. J., E. Cranswick, C. Mueller, and P. Spudich (1982), Source parameters of the 1980 Mammoth Lakes, California, earthquake sequence, *J. Geophys. Res.*, **87**, 4595–4607, doi:10.1029/JB087iB06p04595.

Bergbauer, S., and S. J. Martel (1999), Formation of joints in cooling plutons, *J. Struct. Geol.*, **21**, 821–835, doi:10.1016/S0191-8141(99)00082-6.

Bouchon, M. (1997), The state of stress on same faults of the San Andreas system inferred from near-field strong motion data, *J. Geophys. Res.*, **102**(B6), 11,731–11,744, doi:10.1029/97JB00623.

Boullier, A.-M., K. Fujimoto, T. Ohtani, G. Roman-Ross, E. Lewin, H. Ito, P. Pezard, and B. Ildefonse (2004), Textural evidence for recent co-seismic circulation of fluids in the Nojima fault zone, Awaji island, Japan, *Tectonophysics*, **378**, 165–181, doi:10.1016/j.tecto.2003.09.006.

Brace, W. F., and J. Byerlee (1966), Stick-slip as a mechanism for earthquakes, *Science*, **153**, 990–992, doi:10.1126/science.153.3739.990.

Bürgmann, R., and D. D. Pollard (1992), Influence of the state of stress on the brittle-ductile transition in granitic rock: Evidence from fault steps in the Sierra Nevada, *Calif. Geol.*, **20**, 645–648.

Bürgmann, R., D. D. Pollard, and S. J. Martel (1994), Slip distributions on faults; effects of stress gradients, inelastic deformation, heterogeneous host-rock stiffness, and fault interaction, *J. Struct. Geol.*, **16**, 1675–1690, doi:10.1016/0191-8141(94)90134-1.

Christiansen, P. P., and D. D. Pollard (1997), Nucleation, growth and structural development of mylonitic shear zones in granitic rock, *J. Struct. Geol.*, **19**, 1159–1172, doi:10.1016/S0191-8141(97)00025-4.

Cowan, D. (1999), Do faults preserve a record of seismic slip?—a field geologist's opinion, *J. Struct. Geol.*, **21**, 995–1001, doi:10.1016/S0191-8141(99)00046-2.

Cowie, P. A., and Z. K. Shipton (1998), Fault tip displacement gradients and process zone dimensions, *J. Struct. Geol.*, **20**, 983–997, doi:10.1016/S0191-8141(98)00029-7.

Di Toro, G., and G. Pennacchioni (2005), Fault plane processes and mesoscopic structure of a strong-type seismogenic fault in tonalites (Adamello batholith, Southern Italian Alps), *Tectonophysics*, **402**, 55–80, doi:10.1016/j.tecto.2004.12.036.

Di Toro, G., G. Pennacchioni, and G. Teza (2005), Can pseudotachylites be used to infer earthquake source parameters? An example of limitations in the study of exhumed faults, *Tectonophysics*, **402**, 3–20, doi:10.1016/j.tecto.2004.10.014.

Di Toro, G., T. Hirose, S. Nielsen, G. Pennacchioni, and T. Shimamoto (2006), Natural and experimental evidence of melt lubrication of faults during earthquakes, *Science*, **311**, 647–649, doi:10.1126/science.1121012.

Eshelby, J. D. (1957), The determination of the elastic field of an ellipsoidal inclusion and related problems, *Proc. R. Soc. London, Ser. A*, **241**, 376–396.

Flügge, W. (1967), *Viscoelasticity*, Springer, New York.

Gercek, H. (2007), Poisson's ratio values for rock, *Int. J. Rock Mech. Min. Sci.*, **44**, 1–13, doi:10.1016/j.ijrmms.2006.04.011.

Griffith, W. A., G. Di Toro, G. Pennacchioni, and D. Pollard (2008), Thin pseudotachylites in faults of the Mt. Abbot quadrangle, Sierra Nevada California: Physical constraints on seismic slip, *J. Struct. Geol.*, **30**, 1086–1094, doi:10.1016/j.jsg.2008.05.003.

Guo, H. A., A. Lerner-Lam, and S. E. Hough (1992), Empirical Green's function study of Loma Prieta aftershocks: Evidence for fault zone complexity, *Seismol. Res. Lett.*, **63**, 76.

Hanks, T. C. (1982), f_{max} , *Bull. Seismol. Soc. Am.*, **71**, 1867–1879.

Hough, S. E., and J. G. Anderson (1988), High-frequency spectra observed at Anza, California: Implications for Q factor, *Bull. Seismol. Soc. Am.*, **78**, 692–707.

Ide, S., and G. Beroza (2001), Does apparent stress vary with earthquake size?, *Geophys. Res. Lett.*, **28**, 3349–3352, doi:10.1029/2001GL013106.

Imanishi, K., and W. L. Ellsworth (2006), Source scaling relationships of microearthquakes at Parkfield, CA, determined using the SAFOD pilot hole seismic array, in *Earthquakes: Radiated Energy and the Physics of Faulting*, *Geophys. Monogr. Ser.*, vol. 170, edited by R. Abercrombie et al., pp. 81–90, AGU, Washington, D.C.

Kanamori, H. (1994), Mechanics of earthquakes, *Annu. Rev. Earth Planet. Sci.*, **22**, 207–237, doi:10.1146/annurev.22.050194.001231.

Kanamori, H., and D. L. Anderson (1975), Theoretical basis of some empirical relations in seismology, *Bull. Seismol. Soc. Am.*, **65**, 1073–1095.

Kanamori, H., J. Mori, and T. H. Heaton (1990), The 3 December 1988, Pasadena Earthquake ($M_L = 4.9$) recorded with the very broadband system in Pasadena, *Bull. Seismol. Soc. Am.*, **80**, 483–487.

Kanamori, H., J. Mori, E. Hauksson, T. H. Heaton, L. K. Hutton, and L. M. Jones (1993), Determination of earthquake energy release and M_L using TERRASCOPE, *Bull. Seismol. Soc. Am.*, **2**, 330–346.

- Kattenhorn, S. A., and D. D. Pollard (2001), Integrating 3D seismic data, field analogs and mechanical models in the analysis of segmented normal faults in the Wytch Farm oilfield, southern England, *AAPG Bull.*, **85**, 1183–1210.
- Keilis-Borok, V. I. (1959), On the estimation of the displacement in an earthquake source and of source dimensions, *Ann. Geophys.*, **12**, 205–214.
- Kirkpatrick, J. D., and Z. K. Shipton (2008), Spatial and temporal heterogeneity of exhumed seismogenic faults; implications for seismic slip, *Geophys. Res. Abstr.*, **10**, EGU2008-A-09,126.
- Kirkpatrick, J. D., Z. K. Shipton, J. P. Evans, S. Mickelthwaite, S. J. Lim, and P. McKillop (2008), Strike-slip fault terminations at seismogenic depths: The structure and kinematics of the Glacier Lakes fault, Sierra Nevada United States, *J. Geophys. Res.*, **113**, B04304, doi:10.1029/2007JB005311.
- Lockwood, J. P., and P. A. Lydon (1975), U. S. geologic map of the Mount Abbot quadrangle, California, *Geol. Quadrangle Map GC-1155*, scale 1:62,500, U. S. Geol. Surv., Reston, Va.
- Madariaga, R. (1976), Dynamics of an expanding circular fault, *Bull. Seismol. Soc. Am.*, **66**(3), 639–666.
- Madariaga, R. (1977), Implications of stress-drop models of earthquakes for the inversion of stress drop from seismic observations, *Pure Appl. Geophys.*, **115**, 301–315, doi:10.1007/BF01637111.
- Maerten, L., and D. D. Pollard (2001), Three-dimensional digital field mapping of the Chimney Rock fault system, central Utah, *J. Struct. Geol.*, **23**, 585–592, doi:10.1016/S0191-8141(00)00142-5.
- Maerten, L., E. J. M. Willemse, D. D. Pollard, and K. Rawnsley (1999), Slip distributions on intersecting normal faults, *J. Struct. Geol.*, **21**, 259–272, doi:10.1016/S0191-8141(98)00122-9.
- Maerten, L., D. D. Pollard, and F. Maerten (2001), Digital mapping of three-dimensional structures of the Chimney Rock fault system, central Utah, *J. Struct. Geol.*, **23**, 585–592.
- Manighetti, L., G. C. P. King, Y. Gaudemer, C. H. Scholz, and C. Doubre (2001), Slip accumulation and lateral propagation of active normal faults in Afar, *J. Geophys. Res.*, **106**, 13,667–13,696, doi:10.1029/2000JB900471.
- Manighetti, L., M. Campillo, C. G. Sammis, P. M. Mai, and G. King (2005), Evidence for self-similar, triangular slip distributions on earthquakes: Implications for earthquake and fault mechanics, *J. Geophys. Res.*, **110**, B05302, doi:10.1029/2004JB003174.
- Martel, S. J. (1990), Formation of compound strike-slip fault zones, Mount Abbot quadrangle, California, *J. Struct. Geol.*, **12**, 869–882, doi:10.1016/0191-8141(90)90060-C.
- Martel, S. J., and D. D. Pollard (1989), Mechanics of slip and fracture along small faults and simple strike-slip fault zones in granitic rock, *J. Geophys. Res.*, **94**, 9417–9428, doi:10.1029/JB094iB07p09417.
- Martel, S. J., D. D. Pollard, and P. Segall (1988), Development of simple strike-slip fault zones, Mount Abbot Quadrangle, Sierra Nevada, California, *Geol. Soc. Am. Bull.*, **100**, 1451–1465, doi:10.1130/0016-7606(1988)100<1451:DOSSSF>2.3.CO;2.
- Munguia, L., and J. N. Brune (1984), High stress drop events in the Victoria, Baja California earthquake swarm of 1978, *Geophys. J. R. Astron. Soc.*, **76**, 725–752.
- Mutlu, O., and D. D. Pollard (2008), On the patterns of wing cracks along an outcrop scale flaw: A numerical modeling approach using complementarity, *J. Geophys. Res.*, **113**, B06403, doi:10.1029/2007JB005284.
- Nadeau, R. M., and L. R. Johnson (1998), Seismological studies at Parkfield VI: Moment release rates and estimates of source parameters for small repeating earthquakes, *Bull. Seismol. Soc. Am.*, **88**, 790–814.
- Pachell, M. A., and J. P. Evans (2002), Growth, linkage, and termination processes of a 10-km-long, strike-slip fault in jointed granite: The Gemini fault zone, Sierra Nevada, California, *J. Struct. Geol.*, **24**, 1903–1924, doi:10.1016/S0191-8141(02)00027-5.
- Pennacchioni, G. (2005), Controls on the geometry of precursor brittle structures on the type of ductile shear zone in the Adamello tonalities, Southern Alps (Italy), *J. Struct. Geol.*, **27**, 627–644, doi:10.1016/j.jsg.2004.11.008.
- Prejean, S. G., and W. L. Ellsworth (2001), Observations of earthquake source parameters at 2 km depth in the Long Valley Caldera, Eastern California, *Bull. Seismol. Soc. Am.*, **91**, 165–177, doi:10.1785/0120000079.
- Ramsay, J. G. (1980), The crack-seal mechanism of rock deformation, *Nature*, **284**, 135–139, doi:10.1038/284135a0.
- Richardson, E., and T. H. Jordan (2002), Seismicity in deep gold mines of South Africa: Implications for tectonic earthquakes, *Bull. Seismol. Soc. Am.*, **92**, 1766–1782, doi:10.1785/0120000226.
- Sammis, C. G., R. M. Nadeau, and L. R. Johnson (1999), How strong is an asperity?, *J. Geophys. Res.*, **104**(B5), 10,609–10,619, doi:10.1029/1999JB900006.
- Scholz, C. H. (2002), *The Mechanics of Earthquakes and Faulting*, 471 pp., Cambridge Univ. Press, Cambridge, U.K.
- Segall, P., and D. D. Pollard (1980), Mechanics of discontinuous faults, *J. Geophys. Res.*, **85**, 4337–4350, doi:10.1029/JB085iB08p04337.
- Segall, P., and D. D. Pollard (1983a), Nucleation and growth of strike slip faults in granite, *J. Geophys. Res.*, **88**, 555–568, doi:10.1029/JB088iB01p00555.
- Segall, P., and D. D. Pollard (1983b), Joint formation in granitic rock of the Sierra Nevada, *Geol. Soc. Am. Bull.*, **94**, 563–575, doi:10.1130/0016-7606(1983)94<563:JFIGRO>2.0.CO;2.
- Segall, P., and C. Simpson (1986), Nucleation of ductile shear zones on dilatant fractures, *Geology*, **14**, 56–59, doi:10.1130/0091-7613(1986)14<56:NODSZO>2.0.CO;2.
- Segall, P., E. H. McKee, S. J. Martel, and B. D. Turrin (1990), Late Cretaceous age of fractures in the Sierra Nevada batholith, *Calif. Geol.*, **18**, 1248–1251.
- Shipton, Z. K., A. K. Soden, J. P. Kirkpatrick, A. M. Bright, and R. J. Lunn (2006), How thick is a fault? Fault displacement-thickness scaling revisited, in *Earthquakes: Radiated Energy and the Physics of Faulting*, *Geophys. Monogr. Ser.*, vol. 170, edited by R. Abercrombie et al., pp. 193–198, AGU, Washington, D.C.
- Sibson, R. H. (1975), Generation of pseudotachylite by ancient seismic faulting, *Geophys. J. R. Astron. Soc.*, **43**, 775–794.
- Sibson, R. H. (1985), Stopping of earthquake ruptures at dilational fault jogs, *Nature*, **316**, 248–251, doi:10.1038/316248a0.
- Sibson, R. H. (1986), Brecciation processes in fault zones: Inferences from earthquake rupturing, *Pure Appl. Geophys.*, **124**, 159–175, doi:10.1007/BF00875724.
- Sibson, R. H., and V. G. Toy (2006), The habitat of fault-generated pseudotachylite: Presence vs. absence of friction-melt, in *Earthquakes: Radiated Energy and the Physics of Faulting*, *Geophys. Monogr. Ser.*, vol. 170, edited by R. Abercrombie et al., pp. 153–166, AGU, Washington, D.C.
- Walsh, J. J., and J. Watterson (1988), Analysis of the relationship between displacements and dimensions of faults, *J. Struct. Geol.*, **10**, 239–247, doi:10.1016/0191-8141(88)90057-0.
- Willemse, E. J. M. (1997), Segmented normal faults; correspondence between three-dimensional mechanical models and field data, *J. Geophys. Res.*, **102**, 675–692, doi:10.1029/96JB01651.

W. A. Griffith and S. Nielsen, Istituto Nazionale di Geofisica e Vulcanologia, Via di Vigna Murata 605, I-00143 Roma, Italy. (griffith@ingv.it; nielsen@ingv.it)

D. D. Pollard, Department of Geological and Environmental Sciences, Stanford University, Stanford, CA 94305, USA. (dpollard@stanford.edu)

G. Di Toro and G. Pennacchioni, Dipartimento di Geoscienze, Università di Padova, Via Giotto 1, I-35137 Padova, Italy. (giulio.ditoro@unipd.it; giorgio.pennacchioni@unipd.it)